Late-stage kinetics of systems with competing interactions quenched into the hexagonal phase

Celeste Sagui and Rashmi C. Desai
Department of Physics, University of Toronto, Toronto, Ontario, Canada M5S 1A7
(Received 12 December 1994)

We study the late-stage kinetics for systems with long-range repulsive and short-range attractive interactions, quenched into the hexagonal phase. The system displays two qualitatively different regimes: a monodisperse hexagonal regime and a polydisperse coarsening regime. In the first regime, the evolution of the system towards the hexagonal order characteristic of the crystal ground state is studied. The mechanisms of defect collision and annihilation are identified, and the temporal evolution of orientational and translational order is described. In the coarsening regime, the results of the simulations closely resemble those obtained for a two-dimensional binary mixture confined to an air-water interface. In this regime the system can be described as a two-dimensional froth, with a strong coupling between its topological and geometrical quantities.

PACS number(s): 61.20.Ja, 64.60.−i, 64.75.+g, 75.70.Kw

I. INTRODUCTION

Competing interactions in systems whose constituents simultaneously experience a long-range repulsive interaction (LRRI) and a short-range attractive interaction lead to the formation of supercrystals. These systems form domains to reduce the energy cost originating from the LRRI. The continued subdivision of domains by the LRRI is balanced by the energetic cost of the formation of interfaces. The modulation period emerges from a balance between the strength of the LRRI and the finite domain-wall energy. Periodic modulations of the magnetization or polarization can be seen in examples such as uniaxial ferromagnetic films [1–5], ferromagnetic surface layers [6], magnetic or dielectric fluids [7–9], and ferroelectrics [10].

Most experiments performed on ferromagnetic films can be represented by a dipolar ferromagnet with uniaxial anisotropy in the geometry of a slab of finite thickness L and infinite extent in the plane. Strongly uniaxial films are required to avoid closure domains and branching in the wall structure. At low temperatures and zero applied field, the film surface breaks into stripe domains due to the competition between exchange and dipolar forces, with a zero net magnetization. In a perpendicular magnetic field the stripes whose magnetization is parallel to the field become wider and above a critical value of the field a first-order phase transition to a hexagonal phase of cylindrical domains known as "bubbles" takes place. At still higher fields, a further transition to a uniformly magnetized phase takes place [4]. Similar behavior has also been seen in magnetizable and polarizable liquids (colloidal suspensions of magnetic or dielectric particles) that are confined with a (nonmagnetizable or nonpolarizable) immiscible fluid between closely spaced parallel plates, with a magnetic or electric field perpendicular to the plates [7–9].

Equivalent to these systems, at least at the level of mean field theory, are two-dimensional binary mixtures of monomolecular amphiphilic films confined to an air-water interface such as Langmuir monolayers [11,12]. The competition between the electrostatic interactions and the short-range attraction due to van der Waals forces is at the origin of the supercrystal phases. The patterns formed in magnetic or dielectric (fluid or solid) films are very similar to those formed in monolayers. The origin of the formation of domains is the same (competition between long-range dipolar forces and short-range attractive forces) and their motion generally is overdamped. Yet, while the magnetic or dielectric patterns obey an essentially deterministic dynamics, the monolayer domains are strongly affected by Brownian motion and the large thermal fluctuations are very important in their dynamics.

All the examples presented so far bear a strong similarity in the sense that they are planar dipolar regions with the dipoles perpendicularly aligned to the planes, controlled by bulk dipole forces and line tension. Yet there are other interesting examples with LRRI not necessarily of dipolar origin, such as cholesteric liquid crystals [13], charge-density waves [14], the primate visual cortex [15], ceramic compounds with a long-range Coulombic interaction [16], block copolymers [17], charged colloidal suspensions [18], and chemical front motion [19].

In this paper we consider a broad class of systems in which a rapid quench from a high-temperature homogeneous state to a temperature much below the critical temperature leads to both phase segregation and supercrystal ordering. In previous work [20–23] we have studied the dynamics of quenched quasi-two-dimensional systems with a scalar order parameter and competing interactions. We denote such systems with conserved (nonconserved) order parameter and a long-range repulsive interaction as model B_L (model A_L) and abbreviate it as MB_L (MA_L).

In this paper we concentrate on the late-stage kinetics for these systems when quenched into the hexagonal phase with cylindrical domains (or disk domains in the two-dimensional case). We report on extensive re-

sults related to late stages which involve defect annealing kinetics. For such model systems, we have found two parameter regimes. In one regime, the "monodisperse hexagonal" regime, the system becomes essentially monodisperse, i.e., the radius distribution function becomes highly peaked on the equilibrium value, and the system seeks the hexagonal order mainly through collision and annihilation of defects. In the other regime, the "coarsening polydisperse" regime, the domains are polydisperse, i.e., the radius distribution function is broad, the system is disordered, and the mean radius grows with time. Furthermore, there is a strong coupling between the coordination number of bubbles and their size. A brief report of some of the results of the monodisperse hexagonal regime has appeared in Ref. [23]. Here we introduce new results for both the coarsening regimes including those that closely reproduce most recent experimental results in monolayer systems [24].

A. Monodisperse hexagonal regime

Quenching a system from a disordered single-phase region of its phase diagram to a point inside its coexistence curve creates a network of topological defects which anneals away as the system orders. The nature of the defects determines the ordering kinetics and depends upon the transition studied. Systems with a scalar order parameter ($m = 1$) form domains of ordered phase separated by domain walls (the relevant topological defect), and evolve so as to decrease the domain-wall energy. Systems with continuous order parameters ($m > 1$) have defect structures as points, lines, and textures. In all cases, the late stages of the phase separation are dominated by the motion of these defects, in a way such that, as time evolves, their density decreases and energy is dissipated. The systems with competing interactions studied in this paper present the interesting feature that for the early stages domain walls are the relevant topological defects, while for the late stages, the specific defects of two-dimensional (2D) solids, dislocations and disclinations, are the relevant topological defects. Consequently, there are two relevant order parameters characteristic of 2D solids: a complex (or $m = 2$) translational order parameter and a complex (or $m = 2$) orientational order parameter.

The 2D solid is characterized by quasi-long-range translational order (with algebraic decay of the density-density correlation function) and long-range order in the orientation of nearest-neighbor bonds. Kosterlitz and Thouless [25] pointed out that a 2D crystal is in the same universality class as the XY model and 2D superfluids and superconductors. Their theory for these systems states that the mechanism driving the phase transition from order to disorder is the unbinding of a dilute gas of vortex pairs. Halperin and Nelson [26] and Young [27] extended the ideas of Kosterlitz and Thouless to 2D solids. Translational order can be destroyed by free dislocations in a dislocation-unbinding transition. The theory of this transition is different from the vortex-unbinding transition because dislocations are not described by a scalar charge but by a Burgers vector **b**. Bound dislocation pairs are generated by thermal fluctuations in a crystal near its melting temperature T_m. These pairs have equal and opposite Burgers vectors and the Kosterlitz-Thouless melting transition is the unbinding of these dislocation pairs into free dislocations, as the density of bound pairs increases enough to screen the interaction between two otherwise bound pairs. For $T > T_m$ the translational correlation function decays exponentially. The liquid above the dislocation-unbinding transition is not isotropic, but characterized by quasi-long-range order in the nearest-neighbor-bond orientations (i.e., algebraic decay of the orientational correlation function). Phases which exhibit this intermediate behavior between liquid and solid phases ("oriented liquids") are called *hexatics*. In the same way that dislocations break up translational order, disclinations break up orientational order. A renormalization-group treatment of the hexatic phase leads to a second Kosterlitz-Thouless transition at $T_i > T_m$ above which disclination pairs unbind to form an isotropic liquid. For $T > T_i$, i.e., in the isotropic liquid phase, both the translational and bond-orientational correlations decay exponentially.

The melting-freezing transition has been studied in systems such as polystyrene colloids [18], hard spheres [28], electrons on liquid He surfaces [29], liquid crystals [30], physisorbed noble gases [31], high-temperature superconductors [32], magnetic garnet films [33,34], etc. Excellent reviews are provided by Nelson [35] and Strandburg [31].

B. Polydisperse coarsening regime

Planar cellular patterns occur in a wide variety of systems [36]: planar soap froths, biological cells, grain growth in metals and ceramics, Bénard-Marangoni convection cells, etc. These systems are characterized by the existence of a topological network of three connectivity and a set of coupled geometrical state variables. The dynamics of the state variables and of the topology are strongly coupled. For instance, in the ideal soap froth the geometrical variables are just the areas of the bubbles of incompressible gas and the network is formed by the boundaries of these bubbles, made of soapy water. Magnetic bubbles and monolayer bubbles belong to this same family of cellular patterns [37].

Seul, Morgan, and Sire [24] have reported polydisperse coarsening behavior in a two-dimensional binary mixture, formed by two amphiphiles within a monomolecular film confined to an air-water interface. The disordered bubble patterns have the properties of cellular patterns or froths [36]. A mathematical description of such polydisperse systems must consider the interdependence of the topological and geometrical degrees of freedom present in all the relevant quantities, such as the joint probability distribution $P_n(A, S_B)$ which is the probability of finding a bubble of area S_B in an n-sided Voronoi cell of area A.

Lewis [38] observed in two-dimensional cellular patterns a linear relation between the average area of a cell and the number of its edges. Rivier and Lissowski

[39] obtained Lewis's empirical law from a maximum entropy analysis, based on the assumption that pattern configurations satisfy general topological constraints rather than energetic constraints. Entropy tends to be a maximum but organized form, given by the existence of space-filling cells, and their corresponding topology imposes constraints. The froth selects a cell distribution of maximal arbitrariness or minimal information compatible with the topological constraints.

The work of Seul *et al.* extended the maximum entropy description of cellular patterns to disordered droplet patterns formed during late-stage coarsening in a two-dimensional binary mixture. They found that the maximal entropy theory explains the nearly Gaussian shape of the droplet radius distribution and the anti-correlation between areas of adjacent droplets. These anticorrelations indicate the existence of charge screening at short distances and the suppresion of large fluctuations in droplet area around the mean. The simulations reported in Sec. III B for a "thin film" and MB_L dynamics strongly resemble these experimental results.

This paper is organized as follows. In Sec. II the model, simulations, and quantities measured are presented. In Sec. III, the results are presented; Sec. III A gives results for monodisperse hexagonal systems and Sec. III B gives results for polydisperse coarsening systems. Section IV is reserved for the conclusions.

II. MODEL AND SIMULATIONS

The simulations carried out in this paper are a continuation of those reported previously [22], but explore the physics at much later times. The free energy functional F is written in dimensionless form as

$$F\{\psi\} = \int d^2r \left[\frac{1}{2}(\nabla\psi)^2 + f(\psi) - h\psi\right] + \frac{\beta}{2}\int\int d^2r d^2r' \psi(\mathbf{x}) g(|\mathbf{x}-\mathbf{x}'|)\psi(\mathbf{x}'). \quad (1)$$

Here h is the dimensionless external field that couples linearly to the order parameter and β gives the strength of the LRRI. The order parameter ψ can be written as $\psi = \psi_0 + \Delta\psi$, where $\Delta\psi$ represents the *fluctuations* about zero mean and ψ_0 is the off criticality. $F\{\psi\}$ contains both an *attractive* square gradient term and a long-range *repulsive* term whose kernel is given by

$$g(|\mathbf{x}-\mathbf{x}'|) = \frac{1}{|\mathbf{x}-\mathbf{x}'|} - \frac{1}{[(\mathbf{x}-\mathbf{x}')^2 + L^2]^{\frac{1}{2}}}, \quad (2)$$

appropriate for a ferromagnetic film of thickness L or a Langmuir monolayer of thickness L. The local free energy has a double-well structure below the critical temperature. In dimensionless form it is $f(\psi) = -\frac{1}{2}\psi^2 + \frac{1}{4}\psi^4$.

The time evolution of such a system following a quench from the high-temperature disordered phase is given by the appropriate Langevin equations:

$$\frac{\partial\psi(\mathbf{x},\tau)}{\partial\tau} = -\frac{(-\nabla^2)^n}{2}\frac{\delta F}{\delta\psi} + \sqrt{\epsilon}\mu(\mathbf{x},\tau), \quad (3)$$

where ϵ is the noise strength and $\mu(\mathbf{x},\tau)$ is the dimensionless thermal noise that satisfies the fluctuation-dissipation relation $\langle\mu(\mathbf{x},\tau)\mu(\mathbf{x}',\tau')\rangle = (-\nabla^2)^n\delta(\mathbf{x}-\mathbf{x}')\delta(\tau-\tau')$. For a system with a conserved (nonconserved) order parameter $n = 1$ ($n = 0$).

The Langevin equation was discretized and numerically simulated using standard pseudospectral methods. Square and rectangular lattices of size 128^2 and 256^2, with periodic boundary conditions, were studied. The ratio of lattice spacing $\Delta x/\Delta y$ was kept at $\sqrt{3}/2$ for rectangular lattices. The simulation parameters are reported in Table I. Quenches below the Kosterlitz-Thouless melting temperature were carried out and considering that $T = 0$ is the fixed point of the evolution, noise was neglected.

To study the topological defects of the triangular lattice, Voronoi constructions are performed. The centers of mass are identified and each center assigned a cell containing all points which are nearest to it. Specifically, one draws the perpendicular bisecting lines joining any two centers. The smallest polygon surrounding a given center is the Voronoi (or Wigner-Seitz) cell corresponding to that center. The construction is clearly unique and it fills space in 2D. The Voronoi construction also imposes on the original centers the structure of a graph [36], by defining unambiguously which centers are nearest neighbors and linked by an edge in the graph. Two centers are linked by an edge in the graph if their Voronoi polyhedra have a face in common. Thus a Voronoi partition of space is the *dual* structure to the graph of disk centers or *triangulation*; there is a one-to-one correspondence between the elements of the Voronoi froth and its dual graph [36]. The Voronoi construction thus identifies the defects expressed in terms of disclinations, or sites with coordination number other than 6. This construction also measures the quantities necessary to probe orientational order, specifically the midpoints of the lines connecting adjacent bubbles (bond centers) and the angles these lines make with respect to the horizontal (bond angles). In these simulations the computer algorithm provided by Allen and Tildesley [40] was used.

The original scalar order parameter field has all the information about the system. However, once the system has formed a disordered liquid of disks with some

TABLE I. Parameters used in simulation. N is the system size. L is the film thickness. β is the LRRI strength. ψ_0 is the off criticality. h is the field. τ_{max} is the maximum time achieved in the simulation. n_{run} is the number of independent quenches.

Run	Model	N	L	β	ψ_0	h	τ_{max}	n_{run}
A	MA_L	256	10	0.22	0.0	0.33	20000	4
B	MB_L	256	10	0.22	0.2	0.0	20000	4
C	MA_L	128	10	0.22	0.0	0.33	20000	9
D	MA_L	256	10	0.34	0.0	0.33	60000	1
E	MB_L	128	10	0.22	0.2	0.0	20000	5
F	MA_L	256	50	0.30	0.0	3.00	20000	2
G	MA_L	256	20	0.36	0.0	0.50	70000	2
H	MB_L	256	0.1	5	0.2	0.0	20000	5
I	MB_L	256	10	0.05	0.2	0.0	20000	5

local orientational order, the definition of two new vectorial order parameters facilitates the description of the evolution of the system towards the crystalline ground state.

Two broken symmetries—long-range translational order and long-range orientational order—distinguish solids from liquids in 3D. The diffraction patterns in x-ray scattering from solids show extended translational order. The crystal translational order parameter is the local Fourier component of the density [35],

$$\rho_{\mathbf{K}}(\mathbf{x}) = e^{i\mathbf{K}\cdot\mathbf{x}}, \tag{4}$$

where $\mathbf{K}$ is a reciprocal lattice vector to the first Bragg peak in the structure factor of the crystal. This order parameter is complex, continuous, and Abelian. In 2D solids there is no long-range order, only quasi-long-range translational order. The mean translational order parameter of the infinite crystal is zero. However, the Halperin-Nelson-Young renormalization-group analysis of the dislocation unbinding transition predicts that its correlation function decays algebraically in space with a temperature-dependent decay exponent:

$$g_K(x) = \left\langle e^{i\mathbf{K}\cdot\mathbf{x}'} e^{-i\mathbf{K}\cdot(\mathbf{x}'-\mathbf{x})} \right\rangle \sim x^{-\eta_K(T)}, \tag{5}$$

where the angular brackets represent an average over all pairs of bubbles whose centers are separated by x and an angular average over the six vectors $\mathbf{K}$ measured from the two-dimensional structure factor. The temperature-dependent decay exponent verifies $1/4 \leq \eta_K(T) \leq 1/3$. This power-law decay leads to power-law singularities (rather than δ-function Bragg peaks) in the structure factor $S(\mathbf{k})$ at the reciprocal lattice points $\{\mathbf{K}\}$. For $\mathbf{k} \simeq \mathbf{K}$

$$S(\mathbf{k}) \sim \frac{1}{|\mathbf{k}-\mathbf{K}|^{2-\eta_K(T)}}. \tag{6}$$

The structure factor in the crystal phase diverges at the smaller reciprocal lattice vectors. Above the Kosterlitz-Thouless melting temperature T_m, the correlation function decays exponentially with a characteristic length $\xi(T)$ which is essentially the distance between dislocations. In the isotropic fluid, for $T > T_i$, the scattering function peaks at a momentum transfer $K' \sim 4\pi/(\sqrt{3}a)$ where a is the average interparticle separation. Since the fluid is isotropic, the intensity and shape of the peak are independent of direction. Thus the scattering pattern is a uniform ring whose width is inversely proportional to the length scale on which positional correlations between the constituent particles decay. In the hexatic phase, for $T_m < T < T_i$, the peak position and width of the ring of scattering are the same as for the isotropic fluid phase. However, the fluid develops a sixfold modulation in the angular variable, i.e., the angular isotropy is broken. (Because the bond-orientational order is only quasi long ranged, the x-ray diffraction pattern from an infinite hexatic sample would be an isotropic ring. Finite-size effects in simulations and experiments modify this pattern and a sixfold modulation is observed.)

For the simulations, to show the time evolution of translational order, we consider the quantity f_T defined as

$$f_T = \left\langle \left| \frac{1}{N_B} \sum_{i=1}^{N_B} e^{i\mathbf{K}\cdot\mathbf{X}_i} \right| \right\rangle, \tag{7}$$

where $\mathbf{X}_i$ is the center-of-mass coordinate of bubble i, $\mathbf{K}$ is the reciprocal lattice vector to the first Bragg peak, and the sum is over the centers of the N_B disks. The angular brackets denote an average over the six directions in $\mathbf{K}$, and an ensemble average (i.e., an average over initial states).

Crystals also have a broken orientational symmetry related to a particular set of crystallographic axes. Orientational order in 2D is measured via a complex, $\mathbf{x}$-dependent orientational order parameter [35] defined as

$$\psi_6(\mathbf{x}) = e^{i6\theta(\mathbf{x})}, \tag{8}$$

where $\theta(\mathbf{x})$ is the angle made by the line joining two nearest-neighbor sites relative to some reference axis, while $\mathbf{x}$ locates the midpoint of this bond. The quantity $e^{i6\theta}$ is appropriate for studying order in triangular lattices, since one is only interested in bond order modulo $\pi/3$ rotations. It is also a natural measure of bond orientational order in liquids in 2D, where the average coordination number is 6. An operational definition of Eq. (8) is given by [41]

$$\psi_6(\mathbf{X}_i) = \frac{1}{N_i} \sum_{j=1}^{N_i} e^{i6\theta_j(\mathbf{X}_i)}, \tag{9}$$

where $\mathbf{X}_i$ is the center-of-mass coordinate of bubble i and N_i is the number of nearest neighbors of bubble i; the sum is over all the nearest-neighbor bonds.

A quantitative measure of orientational order is provided by the correlation function:

$$g_6(x) = \langle \psi_6^*(\mathbf{x}) \psi_6(\mathbf{0}) \rangle, \tag{10}$$

where the angular brackets represent an average over all pairs of bubbles separated by x and an angular average over $\pi/3$ radian segments. For the definition given in Eq. (9) for the orientational order parameter $\mathbf{x}$ is taken as $\mathbf{X}_i$; the function $g_6(x)$ exhibits oscillations and it is only meaningful to speak about the envelope of $g_6(x)$. In the 2D crystal the orientational correlation function—or its envelope—is constant. The renormalization-group analysis shows that in the hexatic phase for $T_m < T < T_i$ the orientational correlation function decays algebraically with a temperature-dependent decay exponent $0 \leq \eta_6(T) \leq 1/4$. For $T > T_i$, i.e., in the isotropic liquid phase, both the translational and bond-orientational correlations decay exponentially with a characteristic length $\xi_6(T)$ which is essentially the distance between disclinations.

To study the time evolution of the orientational order, we consider the quantity f_6 defined as [41]

$$f_6 = \left| \left\langle \frac{1}{N_i} \sum_{j=1}^{N_i} e^{i6\theta_j(\mathbf{X}_i)} \right\rangle \right|. \tag{11}$$

The definition of the orientational order parameter used in analyzing various experiments [30] is carried out in Fourier space. The equivalent of Eq. (11) is

$$f_6 = \left| \sum_{k,\theta} S(k,\theta)\, e^{i6\theta} \right|, \tag{12}$$

where $S(k,\theta)$ is the normalized structure factor.

Another definition of the orientational order parameter often used is $f_6' = [g_6(0)]^{1/2}$, that is,

$$f_6' = \left\langle \left| \frac{1}{N_i} \sum_{j=1}^{N_i} e^{i6\theta_j(\mathbf{X}_i)} \right|^2 \right\rangle^{\frac{1}{2}}. \tag{13}$$

This second definition, however, is a measure of local order, in the sense that it contains no information about correlations between bonds separated by large distances. Equations (11) and (12) give essentially the same results, while, naturally, Eq. (13) gives higher values. Both definitions give $f_6' = f_6 = 1$ in a perfect crystalline solid.

III. RESULTS

After the system is quenched, it simultaneously segregates in two phases and creates a supercrystal order corresponding to a modulated structure with hexagonal symmetry. Although these processes are simultaneous, the time evolution is characterized by three stages. Immediately after the quench, the system acquires a very complicated morphology of irregular interpenetrating domains that percolate through the system. The early-time stage [22] corresponds to the initial phase segregation and the emergence of polydisperse domains: the instability amplifies the fluctuations present in the initial conditions, saturates them, and forms sharp interfaces. The intermediate-time stage [22] corresponds to the crossover from the maximally unstable wave number that controls the initial fluctuations to the equilibrium wave number. For very thin films or very weak dipolar strengths, the intermediate stage involves a substantial amount of coarsening and the monodisperse phase may not be accessible either computationally or experimentally. For thicker films or higher dipolar strengths the number of domains stays approximately constant and the radius distribution function becomes highly peaked at the equilibrium value. At this point the system is a disordered liquid of monodisperse disks, without global orientational order but with local orientational order. Further evolution of the system towards the crystalline order constitutes the late-time stage [23]. This evolution becomes slow and hampered by the presence of defects. The ordering process is mainly driven by defect collisions. Thus the lattice or topological degrees of freedom are most relevant in this stage.

A. Monodisperse hexagonal systems

Here we report on the results related to monodisperse hexagonal systems, i.e., systems that gain positional and orientational order in time and show a radius distribution function highly peaked on the equilibrium value for late stages.

Immediately after the quench, the system forms a complex pattern of interconnected domains. In a short time, ψ reaches its saturation value in each of the two phases. The domains then evolve through a series of shape changes in which the interconnected morphology gives way to separated domains of irregular shapes. These then proceed to form circular disks. In this section we shall concentrate on systems described by runs A–G (Table I). These systems are essentially monodisperse for times $\tau > 1000$ so that it is possible to study the late-stage dynamics where the system evolves from a disordered liquidlike state of minority phase disk domains towards its final hexagonal crystalline equilibrium state. Our simulations show that, for both system sizes 128^2 and 256^2, during the late stage, the number of disks stays constant for MA_L and decreases slightly for MB_L. Domain-pattern evolution in these systems is characterized by the interplay of collective degrees of freedom and the corresponding topological defects, and the degrees of freedom associated with shape transformations of individual domains (these *geometrical* degrees of freedom are characteristic of modulated phases). The shape transitions of the early stage correspond mainly to the geometrical degrees of freedom of the system, while the evolution from the liquid towards the crystal corresponds mainly to the topological degrees of freedom. The geometrical and topological times are nearly decoupled in MA_L (no shape transformations in the late stage) and they are coupled in MB_L (coalescence events in the late stage). Systems as described in run H, that even for late times continue to coarsen, are considered in Sec. III B. Typical configurations of the MA_L system are shown in Fig. 1.

Voronoi constructions have been used to isolate the topological defects. Disclinations of charge q are charac-

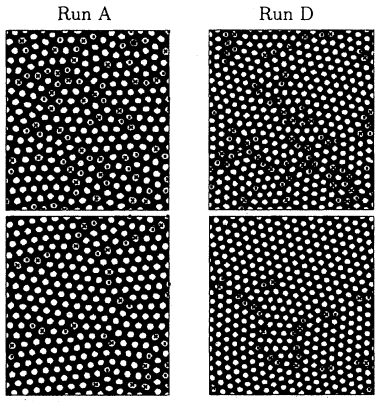

FIG. 1. Configurations for an $N = 256$ MA_L system. The left column corresponds to run A; the top figure is for $\tau = 1000$ and the bottom figure for $\tau = 20\,000$. The right column corresponds to run D (larger β value); the top figure is for $\tau = 1000$ and the bottom figure for $\tau = 60\,000$. This run has a higher dipolar strength. Small solid squares correspond to $z = 5$ and crosses to $z = 7$.

terized by a mismatch of $q\pi/3$ in the orientation angle after a lattice circuit. Alternatively, they can be considered as a site with a wrong number of nearest neighbors as measured by the Voronoi polygon construction. If their coordination number is z and the characteristic coordination number of the lattice is z_0, then their charge can also be expressed as $q = z - z_0$. At late stages, the majority of disks have coordination number $z = 6$, while a smaller number have $z = 5$ (topological charge $q = -1$) and an equal number have $z = 7$ ($q = +1$); the early stages present a small number of disclinations with higher charge. Isolated disclinations with opposite topological charge attract each other strongly and form clusters that correspond to more complex topological defects. The fivefold and sevenfold disclinations often occur in local pairs (nearest neighbors separated by a lattice constant) as edge dislocations. Thus, in a bound pair of dislocations, disclinations are bound in quartets. An edge dislocation corresponds to two additional half rows of bubbles. The Burgers vector is defined as the amount by which a path around the dislocation core fails to close. The direction perpendicular to the line joining the bound-disclination pair is the glide direction, and the Burgers vector (BV) is along this direction. Dislocations move relatively easily in the glide direction, but less easily in the climb direction, perpendicular to the BV.

We have determined and classified the processes by which the topological defects anneal. All of the observed defect collision mechanisms correspond to either a T_1 or a T_2 process [36]. Our simulations show that all the mechanisms involving collision and annihilation (or creation) of defects are different combinations of the elementary T_1 and T_2 processes. Figures 2–7 illustrate the T_1 and T_2 processes, as well as some typical combinations of these processes. Figure 2(a) shows the T_1 process. In the paralellogram formed by k, l, m, and n, the disks of coordination number m and n at the shorter diagonal ends are nearest neighbors, while the other two ($z = l, z = k$) are not. The system achieves a T_1 process by a small displacement of the domains: the ones connected by the shorter diagonal move slightly away from each other

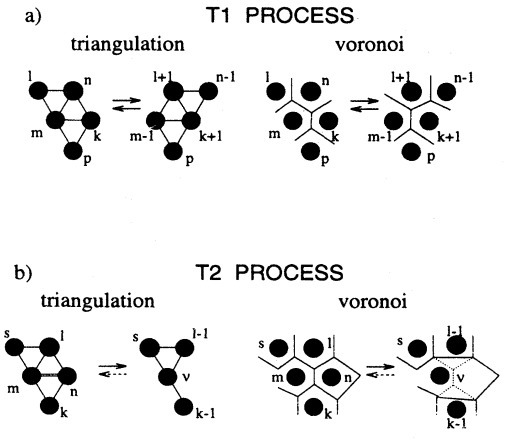

FIG. 2. T_1 and T_2 processes shown in the triangulation and Voronoi representations.

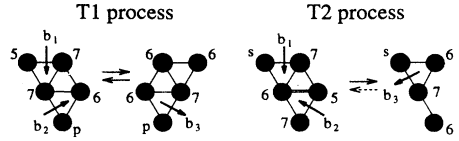

FIG. 3. Examples of the T_1 and the T_2 processes. Both eliminate one 5-7 pair and correspond to collisions among disclinations, unless $p = 5$ and $s = 5$, in which case they involve collisions between dislocations. Only for the latter case are the corresponding Burgers vectors as shown in the diagram relevant.

while the other pair approach each other; as a result the diagonal bond is exchanged. This same process can be visualized using Voronoi constructions. The T_2 process shown in Fig. 2(b) describes two different physical processes which are topologically equivalent. In one case, one of the disks joined by the double line collapses and disappears, as seen, for instance, in stress-induced disorder in magnetic bubble arrays [34]. In the other, the two disks m and n coalesce, a phenomenon which is observed in the simulations of MB_L. In either case, if m and n are the coordination numbers of two such domains, and l, k the coordination numbers of their common neighbors, then, after the T_2 process, the coordination numbers of the common neighbors are $l' = l - 1$ and $k' = k - 1$ and that of the emerging domain is $\nu = m + n - 4$. Such a process conserves charge; the local charge for these four domains before the collision is $q = m+n+l+k-24$ and after the collision, $q' = l' + k' + \nu - 18 = q$. Both T_1 and T_2 processes only involve the four disks m, n, l, k and are independent of neighbors such as p or s. However, these adjacent disks are important in determining whether the process occurring is either a collision between disclinations or between dislocations. For instance, Fig. 3 shows

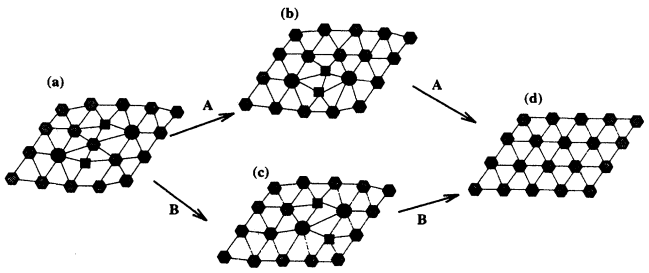

FIG. 4. (a), or equivalently (b), shows an interstitial, i.e., there is an extra site in an otherwise perfect lattice. The configuration in (a) can decay through two equivalent processes. In trajectory **A**, the top dislocation has glided to give (b). A T_2 process consisting in the coalescence of the two fivefold disks (or the elimination of one of the disks) leads to the perfect lattice in (d). In trajectory **B**, a T_2 process consisting in the coalescence of a fivefold and a sixfold disk (or the elimination of the fivefold disk) gives configuration (c), with a virtual pair. The virtual pair decays through a T_1 process to configuration (d) [hexagon, $z = 6$; square, $z = 5$; circle, $z = 7$].

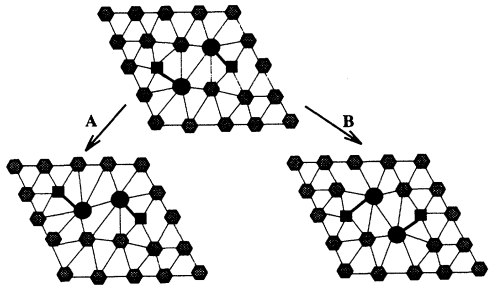

FIG. 5. A vacancy and two related processes: T_2 dislocation climb in trajectory **A** and T_1 rotation of dislocations in trajectory **B**.

a T_1 process in which $m = n = 7$, $l = 5$, and $k = 6$, which results in the annihilation ($\rightarrow$) of a 5-7 pair. The inverse process ($\leftarrow$) creates a 5-7 pair. If $p = 6$ or $p = 7$, the process involves disclinations but if $p = 5$ one can define a collision between dislocations of BV $\mathbf{b_1}$ and $\mathbf{b_2}$ that combine to create a third dislocation $\mathbf{b_3} = \mathbf{b_1} + \mathbf{b_2}$. The inverse process consists of the splitting of the dislocation $\mathbf{b_3}$ to give the dislocations $\mathbf{b_1}$ and $\mathbf{b_2}$. Figure 3 also shows similar behavior ($\rightarrow$) for the T_2 process. If $s = 6$ or $s = 7$, the process involves disclinations but if $s = 5$, it can be considered as collision of the dislocations $\mathbf{b_1}$, $\mathbf{b_2}$ to create the dislocation $\mathbf{b_3} = \mathbf{b_1} + \mathbf{b_2}$. The inverse of such a process would imply a nucleation of a magnetic bubble or a mitosis of a monolayer domain; such processes are less frequent in the systems we are studying. There are conservation laws associated with these mechanisms. T_1 conserves the number of domains and the number of bonds; in a T_2 process one domain and three bonds disappear every time the process takes place. Both processes conserve the topological charge and the BV (when defined).

Dislocations create a strain field and under the influence of this field they tend to cluster and form more complex defects, made up by two or more dislocations. If the net BV of any such cluster of defects is zero (the simplest case being two dislocations with opposite BV) then orientational and translational order is preserved outside a loop that encloses the cluster (if the cluster is small compared to system size). Although many combinations of differently coordinated disks in the T_1 and T_2 diagrams are imaginable, the fact that defects with $|q| > 1$ are not energetically favored reduces the possibilities. Let us designate by δP the number of 5-7 pairs that change in a process (note that a T_2 process eliminates one bubble every time it happens). Here all the processes of defect collision with the constraint $|q| = 1$ are presented. More complicated processes are a concatenation of these "unit" processes.

(I) For the T_1 case, these combinations follow.

(i) $m = 7$, $k = 5$, $l = n = 6$. Dislocation glide: a movement of the dislocation along the direction of its BV, i.e., perpendicular to the line joining the fivefold and sevenfold disks [Figs. 4(a) to 4(b)]. $\delta P = 0$.

(ii) $m = n = 7$, $l = k = 6$ or $m = n = 6$, $l = k = 5$. Rotation of two equal sign disclinations. Let s designate the other common neighbor of l and m and let r designate the other common neighbor of n and k. If $m = n = 7$, $l = k = 6$, and $r = s = 5$; or $m = n = 6$, $l = k = 5$, and $r = s = 7$, this process describes the rotation of two dislocations of opposite BV (Fig. 5B). $\delta P = 0$.

(iii) $m = n = 7$, $l = 5$, $k = 6$; or $m = 6$, $n = 7$, $l = k = 5$. Annihilation of a 5-7 pair. If $m = n = 7$, $l = 5$, $k = 6$, and $p = 5$ (Fig. 3); or $m = 6$, $n = 7$, $l = k = 5$, and $p = 7$, it is a collision of dislocations. $\delta P = -1$.

(iv) $m = n = 7$, $l = k = 5$. Collision of two dislocations of opposite BV. This particular configuration is known as virtual pair, twisted bond, or lattice shear. It only involves a small distortion of the local lattice [Figs. 4(c) to 4(d)]. $\delta P = -2$.

All these processes have their inverse: rotation or glide in the opposite direction, creation of a pair or splitting of a dislocation, or the creation of two dislocations of opposite BV. This last process, the creation of a virtual pair, often occurs as an intermediate stage in which the newly created dislocations combine with other dislocations nearby.

(II) For the T_2 case, the combinations follow.

(i) $m = n = 5$, $l = k = 6$. Rotation of two fivefold disclinations. If $r = s = 7$ (s is the other common neighbor of l and m, and r is the other common neighbor of n and k), this represents the rotation of two dislocations with zero net BV. $\delta P = 0$.

(ii) $m = 5$, $n = 6$, $l = 7$, $k = 6$. Dislocation climb: the dislocation moves along the direction of one of the two excess rows it generates, eliminating one disk in each step, and eventually the whole row (Fig. 5A). $\delta P = 0$.

(iii) $m = 6$, $n = 5$, $l = k = 7$; or $m = n = 5$, $l = 6$, $k = 7$. Annihilation of a 5-7 pair, or recombination of two dislocations if $s = 5$ (Fig. 3) or $s = 7$. $\delta P = -1$.

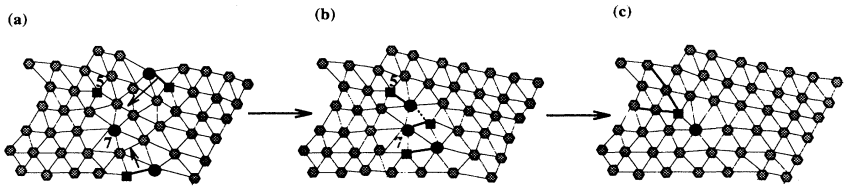

FIG. 6. (a) shows the initial configuration consisting of two dislocations and two second-nearest-neighbor disclinations. The dislocations glide in the directions indicated by the arrows and produce configuration (b). In (b) the top dislocation unbinds to recombine with the isolated disclinations. The elimination of the virtual pair and the glide of the remaining dislocation lead to configuration (c), where the extra half rows associated with the dislocation have been highlighted.

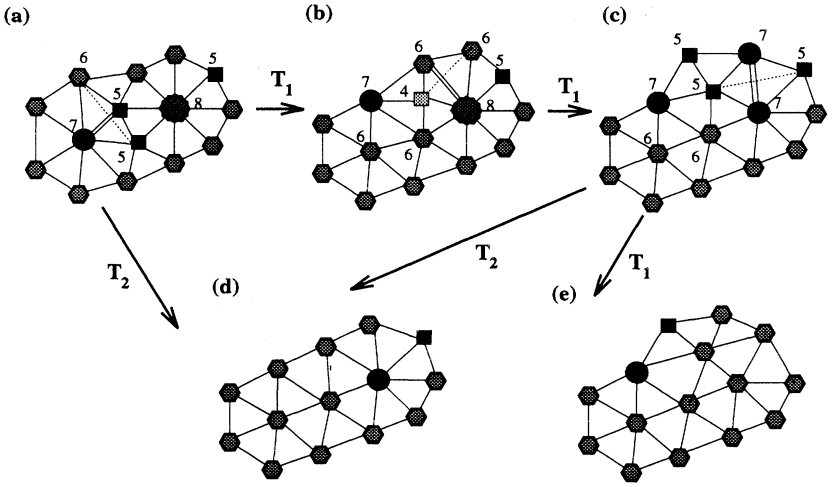

FIG. 7. (a) shows the initial configuration containing a higher-order disclination. A single T_2 process involving the sevenfold, the eightfold, and the two linked fivefold disks leads the system to configuration (d). A chain of T_1 processes [(a) $\rightarrow$ (b)$\rightarrow$ (c)$\rightarrow$ (e)] leads to configuration (e) with one more disk than configuration (d). In (a), (b), and (c) the double and dotted lines denote the bonds that will disappear and be created, respectively. Configuration (c) could also decay into (d) through a T_2 process.

(iv) $m = n = 5$, $l = k = 7$. Collision of two dislocations of opposite BV. This process eliminates an interstitial, i.e., an extra site in an otherwise perfect lattice [Figs. 4(b)–4(d)]. $\delta P = -2$.

(v) $m = 5$, $n = 6$, $l = k = 6$. Creation of a 5-7 pair if $s = 5$ or $s = 6$; or split of a dislocation if $s = 7$. $\delta P = +1$.

All these processes can occur in a variety of combinations. Figures 4 and 5 show two well-known defect structures: an interstitial and a vacancy. These configurations have zero net Burgers vector. The interstitial given in Fig. 4(a) can decay through two equivalent processes: (T_1 dislocation glide plus T_2 elimination of interstitial) or (T_2 dislocation climb plus T_1 elimination of a virtual pair). Figure 5 shows a vacancy, i.e., the absence of an atom in an otherwise perfect lattice. In experimental systems, the dislocations created by the vacancy tend to glide towards grain boundaries. In the absence of the grain boundaries, this defect configuration decays via climb of the associated dislocations.

Figures 6 and 7 show examples of decay of disclinations. In Fig. 6 an initial configuration consisting of two dislocations and two second-nearest-neighbor disclinations decays to a final configuration with a single dislocation via the unbinding and recombination of one of the dislocations. Figure 7 shows an initial configuration with a higher-order disclination decaying through a chain of T_1 processes or through a T_2 process.

For runs A and B and for times between $\tau = 3000$ and $\tau = 20\,000$, collisions between two dislocations (as opposed to collisions between unbound disclinations) represent 92% of all collisions in MA_L and 82% in MB_L (for the late stages, all the collisions occur between two dislocations).

The T_1 and T_2 processes are generally used in the description of polygonal froths [36,42]. The systems studied in this paper can all be described in terms of cellular patterns or froths. However, there are some important differences between the simulations in this section (runs A–G) and the simulations corresponding to run H, presented in the next section. A system such as is described by run H is believed to verify von Neumann's law [37], which states that the area of a froth cell increases with time if $z - 6 > 0$ or decreases if $z - 6 < 0$, $\dot{A} = k(n - 6)$. Instead, in the monodisperse case this area remains constant. Also, in run H, there are higher-order defects even though the average coordination number is still 6, while in the monodisperse case only $z = 6$, 5, or 7 occurs at late times. One of the most important differences is the fact that at late stages the T_2 processes in froths are dominant and the T_1 processes are very rare. In monodisperse hexagonal systems, on the other hand, the T_1 processes are by far the dominant mechanism (it is the only mechanism for MA_L in run A and accounts for 90% of the dislocation annihilations for MB_L in run B).

The simulation results for MA_L bear resemblance to the experimental observations of Seshadri and Westervelt [33]. These authors studied a continuous hexatic-to-liquid melting transition as a function of density in 2D magnetic bubble arrays in garnet films. The bubbles interact with a $1/r^3$ potential. The authors see the hexatic phase with orientational order undergo a phase transition to form an isotropic liquid when dislocations unbind into disclinations. Instead, our system was quenched into the crystalline phase so a continuous process is observed as the system progressively freezes and no parameter is tuned to equilibrate an intermediate phase. However, the freezing evolution of our simulated system proceeds in time in a manner similar—but in the opposite sense—to the melting process described by Seshadri and Westervelt. The system gains orientational and positional order in time as defects decay and the mechanisms of defect collisions are the same.

The time evolution of the system found in the simulations is characteristic of 2D freezing: starting from its liquid state, the system orders both orientationally and positionally towards its crystalline state. To quantify the two types of ordering, we have measured the normalized structure factor $S(k, \theta)$, the orientational order parameter f_6 as defined by Eqs. (11) and (12), which produce essentially the same curve, and the translational order parameter f_T as defined by Eq. (7). We have also measured the concentration of defects $\rho(\tau)$ defined as the ratio of the number of disks with $z \neq 6$ to the total number of disks N_B: $\rho(\tau) = 1 - C_6$, where $C_6 = N_6/N_B$ is the

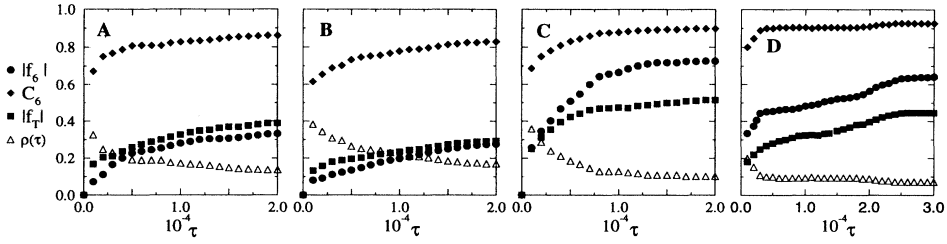

FIG. 8. Time evolution of the orientational order parameter f_6, the concentration of sixfold coordinated disks C_6, the translational order parameter f_T, and the concentration of defects $\rho(\tau)$ for runs A–D.

concentration of sixfold coordinated disks. The orientational order parameter f_6' defined by Eq. (13) produces results that follow closely those for C_6.

Figure 8 shows the time evolution of the orientational and translational order parameters f_6 and f_T, the concentration of sixfold coordinated disks C_6, and the defect concentration $\rho(\tau)$ for runs A–D. Figures 8A and 8B show that the curves that represent f_6, f_T, and C_6 as a function of time in MB_L run nearly parallel to those of MA_L, but with lower values of the ordinate. This is because at any $\tau > 1000$, MB_L has higher defect concentration $\rho(\tau)$, and therefore less order. In MB_L, the maximally unstable wavelength that governs the initial fluctuations is much smaller than the equilibrium wavelength. The conservation law imposes a slower evolution, so that crossover phenomena are still present at late times. Through coalescence, the system tries to eliminate the excess of domains to reach the equilibrium lattice constant. The rather low values of f_6 and f_T for Figs. 8A and 8B suggest that both MA_L ($N = 256$) and MB_L ($N = 256$) are still in the liquid state. In particular, the state of MA_L for $\tau = 20\,000$ (Fig. 1) is found to correspond to the state of a 2D locally oriented fluid, maybe near freezing into a hexatic phase. At this stage, the total concentration of defects is $\rho(\tau) = 13.7\%$ [Fig. 9(a)] and the concentration of unbound 5-7 pairs is 1.3% (these pairs are next-nearest neighbors forming loosely bound disclinations). The orientational correlation length as measured by an exponential fit to $g_6(x)$ is $\xi_6 \simeq 3.5a$, where a is the lattice space. The structure factor has already developed a sixfold modulated pattern, as shown in Fig. 9(b). The defects merge into a network of strings surrounding regions with $z = 6$ of size $\xi_T \simeq 3a$ and randomly oriented with respect to neighboring regions of hexagonal symmetry.

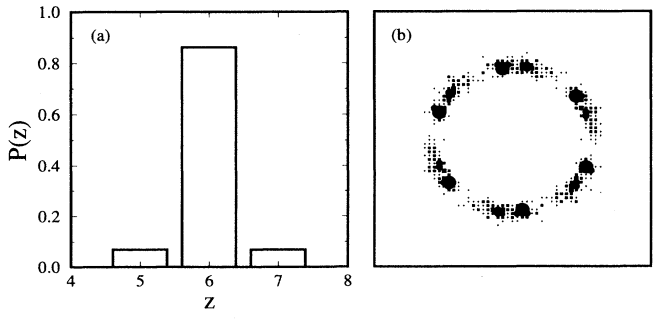

FIG. 9. For run A at $\tau = 20\,000$ (a) probability $P(z)$ that a bubble has z adjacent bubbles, (b) structure factor.

For the sake of comparison, run C is included in Fig. 8C and run D in Fig. 8D. Figure 8C shows a smaller system, an $N = 128$ MA_L system, at $\tau = 20\,000$, while Fig. 8D shows an $N = 256$ MA_L system with higher dipolar strength ($\beta = 0.34$) at $\tau = 60\,000$. Thus both systems are expected to evolve faster than runs A and B. In fact, both systems display a higher amount of orientational order as shown for the latest time available in the simulation. For run C at $\tau = 20\,000$, the concentration of defects is $\rho(\tau) = 10.3\%$ and in only two out of the nine runs did we find one unbound 5-7 pair, where the 5 and 7 were loosely bound (second-nearest neighbors). Estimates of the correlation lengths for the run C system give a translational correlational length $\xi_T \sim 4.5a$ and an orientational correlational length $\xi_6 \sim 12a$. For run D at $\tau = 60\,000$, the concentration of defects is $\rho(\tau) = 7.3\%$. The translational correlational length is $\xi_T \sim 7a$ and the orientational correlational length is $\xi_6 \sim 11a$. One has to be cautious in the analysis of these two runs. For run C we cannot ultimately discard the fact that the small size of the system stabilizes it and induces order. For run D, more runs are needed to improve the statistics.

As the system freezes, it gains both orientational and positional order. Although the data for these Langevin simulations are not conclusive, inspection of the configurations corresponding to various runs indicates that in those runs where grain boundaries are not formed (there may be strings of dislocations but not percolating grain boundaries), the onset of quasi-long-range orientational order occurs sooner than the onset of quasi-long-range positional order. In such cases, the system evolves in time through intermediate stages of hexatic order before reaching the crystalline state. On the other hand, in those runs that do present formation of grain boundaries, the orientational and translational order grow simultaneously. Further simulations using a different approach [43,44] seem to confirm these conclusions. While in real systems the grain boundaries may relax through the external boundaries of the system, in simulations with periodic boundary conditions grain boundaries may be artificially stabilized or may appear in certain geometries (for instance, in more or less parallel pairs or in a single closed loop). A curious example is presented by run G, that represents a very "shallow" quench (very high β is equivalent to shallow temperature quenches). The sequence of pictures in Fig. 10 shows a network of grain boundaries evolving to form a closed loop (considering the domains delimited by the grain boundary, there are obvious finite-size effects). Because this is a very shallow quench, there are more T_2 processes than observed

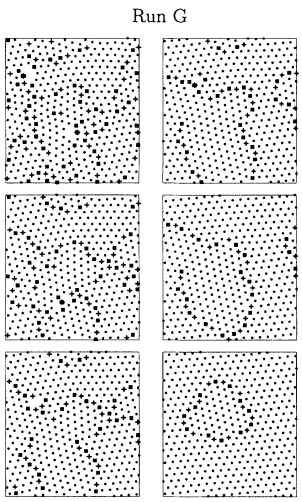

FIG. 10. Time evolution of run G. From top to bottom, the left panel corresponds to configurations at time $\tau = 1000$, 4000, 7000 and the right panel to configurations at time $\tau = 12\,000$, 20 000, 70 000.

for MA_L in the other runs. At $\tau = 60\,000$ the system has developed a (shrinking) circular loop that forms the boundary between two regions of different orientation. These regions have both translational and orientational order.

Finally, Fig. 11 shows a logarithmic plot of the defect concentration $\rho(\tau)$ for runs A and B. An exponent of 0.34 ± 0.06 is measured. The remaining runs, C–G, give nearly the same exponent. A general argument about decay of defects goes as follows [45,46]. Suppose L is the characteristic linear dimension of the ordered domains that compete to select the ground state. Let $V(L)$ be the potential that characterizes the interaction of the relevant defects. The motion of defects in the simplest case is characterized by a Langevin equation, $dL/d\tau \sim -dV(L)/dL$. Point defects in 2D interact logarithmically, so the integration of the Langevin equation gives $L(\tau) \sim \tau^{1/2}$. (In 2D, for order parameters with two components there is a logarithmic correction [47] $L(\tau) \sim (\tau/ln\tau)^{1/2}$.) Assuming that the defects are uniformly distributed, the concentration of defects verifies $\rho(\tau) \sim [L(\tau)]^{-2} \sim \tau^{-1}$. A decay exponent ~ 1 has been observed repeatedly in simulations [45,46,48]. In spite of our previous speculations [23], at present we believe that the expected value of the decay exponent is 1/2. The reason for this is that dislocations in our simulations are not distributed uniformly in regions of linear dimension L but rather on the surface or the contour of this region; this is the case even if they do not form grain boundaries. Thus we expect $\rho(\tau) \sim [L(\tau)]^{-1} \sim \tau^{-1/2}$. Still, we measure 0.34 and this could be due to the transients of the "early-time" behavior. For instance, Mondello and Goldenfeld [49] studied the dynamics of a system with a nonconserved complex order parameter following a deep quench. They found an effective value of the dynamical exponent at early times, $L(\tau) \sim \tau^{0.37}$, and at later times they observed a crossover to $L(\tau) \sim \tau^{1/2}$. Further simulations or experimental studies addressing this particular issue of crystallization would help to elucidate this point.

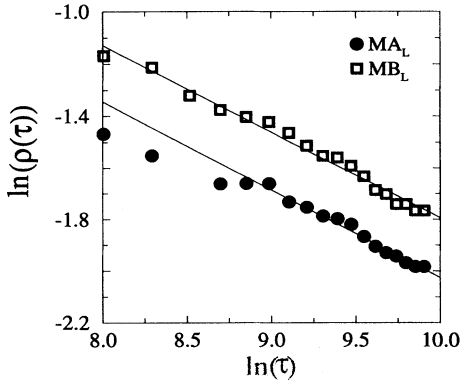

FIG. 11. Log-log plot of the decay of the defect concentration $\rho(\tau)$ for runs A and B.

B. Polydisperse coarsening systems

Here we report on the results related to run H, i.e., MB_L for a thin film. In this run, the parameters are chosen so that as far as the simulations ran, the system is coarsening and verifies a growth law $\langle R \rangle \sim t^n$ for the mean radius. The simulations in this parameter regime strongly resemble the experimental results obtained by Seul, Morgan, and Sire (SMS) [24] for a Langmuir monolayer.

Figure 12 shows configurations for MB_L for runs B, I, and H, and for model B without LRRI ($\beta = 0$). While the systems represented by run B are essentially monodisperse at $\tau = 1000$, those represented by run H clearly show coarsening at very late times. Run I, on the other hand, shows an intermediate behavior between runs B and H. The configurations obtained for run H and model B are very similar, the only difference is that run H presents fewer coalescence events than model B.

Figure 13 shows the scaled normalized domain radius distribution $f(R/\langle R \rangle)$ for runs B, I, and H. The droplet distribution function in run B evolves from a flat, broad distribution to a narrow, peaked one. In run I the distribution narrows slowly in time. On the other hand, the distribution function in run H is relaxing in time to a broader, more symmetric shape. SMS found that the experimental radius distribution for the coarsening monolayer approximates a Gaussian shape and computed an analytical expression by integrating over a and summing over n the probability distribution $P_n(a, s)$ given by Eq. (21) below. In run H there is some indication of scaling for times $\tau > 10\,000$. Coalescence processes become rarer after $\tau = 10\,000$. Thus scaling could only be achieved at late stages, when the only mechanism of droplet growth and dissolution is diffusion of material from small droplets to large droplets. A careful study of scaling would have to probe much later times (and thus larger systems) than are probed in these simulations. We

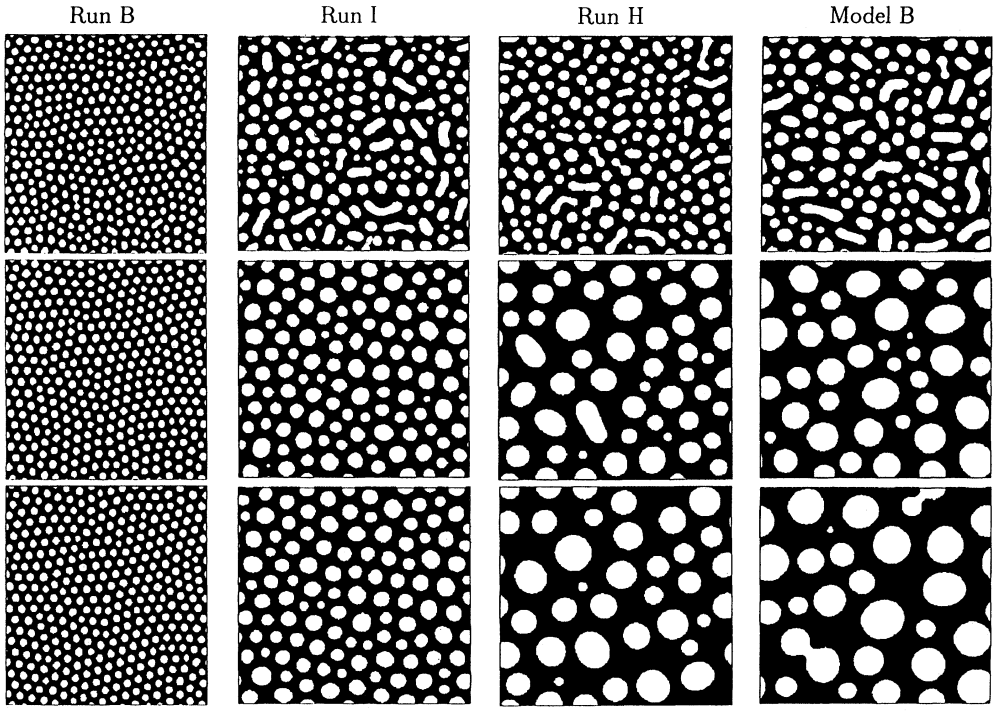

FIG. 12. Configurations showing the time evolution for runs B, I, H and for model B (no LRRI, $\beta = 0$, $\psi_0 = 0.2$). From top to bottom the times shown for all runs are $\tau = 1000$, 10 000, and 20 000.

have also simulated model B without LRRI for the same volume fraction ($V_f = 0.40$, $\psi_0 = 0.2$). However, for this volume fraction model B has not reached the scaling regime at the times probed either.

Figure 14(a) shows the mean radii of runs B, I, and H, while Fig. 14(b) shows a logarithmic plot of the mean radius for runs I and H and the corresponding fits. Growth exponents of $n \sim 0.10$ and $n \sim 0.25$ are measured. For model B with the same volume fraction, the effective growth exponent for the mean radius at the same time is $n \sim 0.23$ (i.e., this high volume fraction requires much longer times to reach the scaling regime typical of model B, for which the growth exponent is $n = 1/3$ [50]).

Now we review the main features of the maximum entropy formalism as introduced by Rivier [39] and extended by SMS. The results of this analysis will be applied to our simulation results. Let $\langle S_B \rangle$ and $\langle A \rangle$ be the average droplet area ($\langle S_B \rangle \sim t^{2n}$) and the average Voronoi cell area. Let $P_n(a,s)$ be the probability of finding a bubble of area $S_B = s\langle S_B \rangle$ in an n-sided Voronoi cell of area $A = a\langle A \rangle$ (thus $\langle a \rangle = 1$ and $\langle s \rangle = 1$). Let p_n be the density of n-sided Voronoi cells: $p_n = \int da\, ds P_n(a,s)$, and a_n and s_n be the averages of a and s for these cells: $a_n = \frac{1}{p_n} \int da\, ds\, a\, P_n(a,s)$, idem for s_n. The entropy is defined as

$$S = -\sum_n \int da\, ds\, P_n(a,s) \ln[P_n(a,s)/P_0(a,s)], \quad (14)$$

where $P_0(a,s) \sim (as)^d$ accounts for the fact that at least $(d+1)$ points are needed to define a cell in d dimensions. The maximization of entropy has to be carried out subject to the following constraints, for the $2-d$ system.

(i) Normalization of probability:

$$\sum_{n \geq d+1} p_n = 1. \quad (15)$$

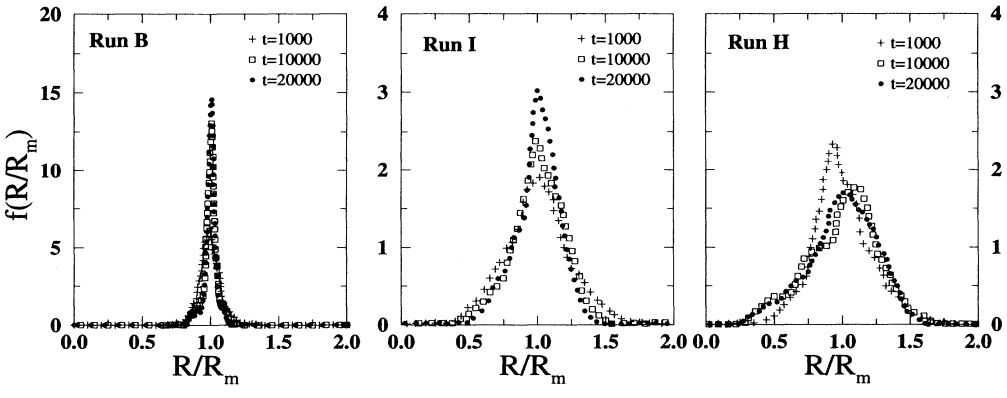

FIG. 13. Droplet distribution function for runs B, I, H.

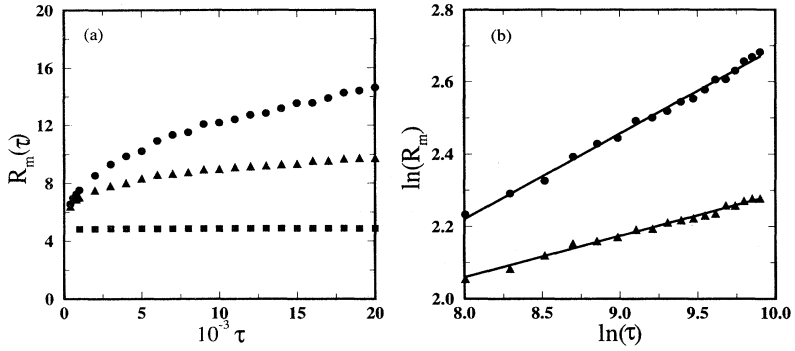

FIG. 14. (a) Time evolution of the mean radius for runs B (squares), I (triangles), and H (circles). (b) Logarithmic plot for the mean radius in runs H and I, and corresponding fits.

(ii) Space-filling froth structure:

$$\sum_{n\geq d+1} p_n a_n = 1. \tag{16}$$

(iii) Charge neutrality:

$$\sum_{n\geq d+1} p_n (n-6) = 0. \tag{17}$$

This last constraint is a consequence of the Euler-Poincaré theorem relating the number of cells, edges, and vertices covering a two-dimensional manifold [39]. Since the charge of an n-sided cell is defined as $q = n - 6$, this constraint ensures global charge neutrality, $\langle q \rangle = 0$.

These are the most common topological constraints. An additional constraint is given by assigning a thermodynamic energy functional to the froth [51]. The simplest form it can have is quadratic in $n - 6$, so that in a relaxed froth it favors all coordination numbers equal to 6. If the moments of the distribution p_n are defined as $\mu_\alpha = \sum_{n\geq d+1} p_n (n-6)^\alpha$ ($\mu_0 = 1$ and $\mu_1 = 0$), the conservation of energy is equivalent to fixing the second moment of the distribution.

(iv) Conservation of energy:

$$\sum_{n\geq d+1} p_n (n-6)^2 = \mu_2. \tag{18}$$

As stated by SMS, since the constraint Eq. (18) is linearly coupled to the entropy Eq. (14) via a Lagrange multiplier, entropy maximization is equivalent to minimization of an effective free energy $F = \mu_2 - \hat{T}S$, where the effective temperature $\hat{T}$ is fixed by the value of μ_2. All of these are topological constraints valid for the Voronoi froth. In addition, the presence of droplets introduces a constraint to account for the presence of constant volume fraction V_f.

(v) Conservation of mass:

$$\sum_{n\geq d+1} p_n s_n = 1. \tag{19}$$

The final constraint establishes that the area of a droplet cannot exceed that of its associated Voronoi cell.

(vi) Each Voronoi cell contains exactly one droplet:

$$V_f s_n < a_n. \tag{20}$$

Introducing the Lagrange multipliers γ_a, γ_s, γ_1, and γ_2 for each constraint and taking the functional derivative of S, the probability is expressed as

$$P_n(a,s) = \theta(a_n - V_f s_n)\frac{(as)^2}{Z} \times \exp\{-[\gamma_a a + \gamma_s s + \gamma_1 (n-6) + \gamma_2 (n-6)^2]\} \tag{21}$$

where θ is the step function and Z is given by

$$Z = \sum_{n\geq d+1} \int da\, ds \theta(a_n - V_f s_n)(as)^2 \times \exp\{-[\gamma_a a + \gamma_s s + \gamma_1 (n-6) + \gamma_2 (n-6)^2]\}. \tag{22}$$

One can maximize the entropy as a function of a_n and s_n with the given constraints. If these constraints are relaxed, then there is more arbitrariness in the distribution $\{p_n\}$. Rivier *et al.* showed that Lewis's law corresponds to "maximal arbitrariness" in this distribution, obtained by making one of the constraint equations a linear combination of the others. Thus one can write

$$a_n = 1 + \lambda_a (n-6) + \nu_a [(n-6)^2 - \mu_2], \tag{23}$$

$$s_n = 1 + \lambda_s (n-6) + \nu_s [(n-6)^2 - \mu_2]. \tag{24}$$

In cells with strong energetic constraints, the quadratic term is expected to dominate while in coarsening droplet patterns, ν_a and ν_s are expected to give a negligible contribution (Lewis's law is just the linear part of these equations). In a different study of the late-stage kinetics for systems quenched in the hexagonal phase, we found some cases where the quadratic term is also important [44].

Finally, to finish this theoretical overview, we consider the Aboav-Weaire law [36]. This law describes the correlations in the topological charge of nearest-neighbor cells. If $q = n - 6$ is the topological charge of an n-sided cell and q_{NN} is the average charge of its n nearest-neighbor cells (so that the total topological charge of the cell and its neighbors is $q + nq_{NN}$) then the Aboav-Weaire law states that $q + nq_{NN} = (1 - a)q + \mu_2$. The average of this relation, $\langle q + nq_{NN} \rangle = \mu_2$ (since $\langle q \rangle = 0$), shows that at the nearest-neighbor level charge compensation

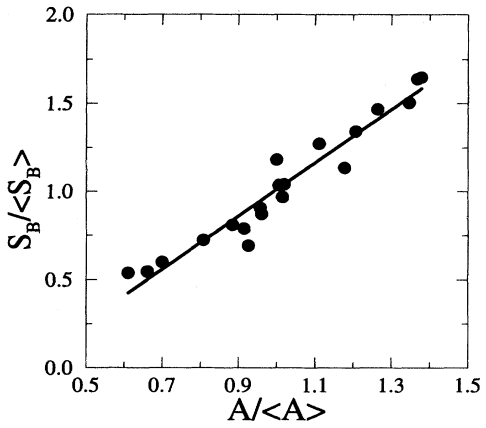

FIG. 15. Correlations between normalized areas of droplets and normalized areas of the corresponding Voronoi cells in run H. The linear fit has a slope of 1.5.

is not complete. For most physical systems verifying the Aboav-Weaire law, $a \geq 1$. From the Aboav-Weaire law it is seen that topological charge is screened at short range by minimizing the net topological charge of the group formed by the cell and its nearest neighbors with respect to the average μ_2. This is equivalent to setting $a = 1$. Alternatively, if $m(n)$ is the average coordination number of the n nearest-neighbor cells of the n-sided cell, the Aboav-Weaire law reads

$$\sum_{n \geq d+1} nm(n)p_n = 36 + \mu_2. \tag{25}$$

This relation has also been obtained for a system where there is no correlation in cell shapes beyond nearest neighbors and where all the elementary transformations T_1, T_2 mitosis and their inverses are allowed [52]. The Aboav-Weaire law is found as an equation of the equilibrium state.

Run H at $\tau = 20\,000$ gives $p_6 \simeq 49.64\%$, $p_5 = p_7 \simeq 22.30\%$, and $p_4 = p_8 \simeq 2.88\%$. The second moment is $\mu_2 = 0.68$ and the coefficients of Lewis's law are $\lambda_s = 0.22$ and $\lambda_a = 0.14$. As time evolves, p_6 tends to decrease while $p_{n \neq 6}$ tends to increase. This is because the system has not quite reached the scaling regime, where p_n is expected to be constant. In fact, for $\tau > 13\,000$, the p_n's are nearly constant. For comparison, the experimental values obtained by SMS are $p_6 \simeq 45\%$, $p_5 = p_7 \simeq 25\%$, and $p_4 \simeq p_8 \simeq 2.5\%$, $\lambda_s \simeq 0.23$, $\lambda_a = 0.15$, and $\mu_2 \simeq 0.64$. The growth exponent they measure is $n \simeq 0.28$.

While at low volume fractions s and a are essentially uncorrelated so that the average $\bar{s}(a)$ is independent of a, for larger volume fractions a plot of $\bar{s}(a)$ vs a shows a linear correlation between bubble and cell areas, as shown in Fig. 15 for run H where a slope of $\simeq 1.5$ is measured. This implies $\lambda_s = 1.5\lambda_a$, in good agreement with the values of λ_s and λ_a found, as well as with the experimental values.

Figure 16 shows Lewis's law and Aboav-Weaire law for run H. The linear dependence is quite apparent. SMS considered that the parameter λ_s is a susceptibility that determines the change in the average droplet area due to a change in the coordination number (or equivalently, the magnitude of the geometrical response due to variations of a topological quantity). They concluded that, due to the linear correlation between droplet areas and topological charge, the screening of charge precludes large fluctuations in the area of the droplet.

Figure 17 shows the spatial correlations in the areas of nearest-neighbor droplets for run H. There is a strong anticorrelation due to the screening of charge and of area fluctuations. The solid line corresponds to the function

$$\frac{s'}{s} = \frac{1}{s}\left[1 + \frac{a(1-s) + \lambda_s \mu_2}{6 + (s-1)/\lambda_s}\right] \tag{26}$$

provided by SMS. This expression comes from eliminating n from Lewis's law, $s = 1 + \lambda_s(n-6)$, and inserting its expression into Aboav-Weaire law; s' is the average fractional droplet area of the nearest-neighbor droplets. For the fit $a = 1$ was set.

Our simulation results for run H are in close agreement with the experimental results for the two-dimensional binary mixture during late-stage coarsening. There remains the question of why runs B and H show such different behavior. The model presented here reproduces very well the ordering mechanism in the case of monodisperse hexagonal systems and the coarsening mechanism in the case of polydisperse systems. However, here we are confronted with the question of whether there actually exists an equilibrium radius R_{eq} for the coarsening system so that for sufficiently long times the system will cross over to an ordered state, or whether there is not a

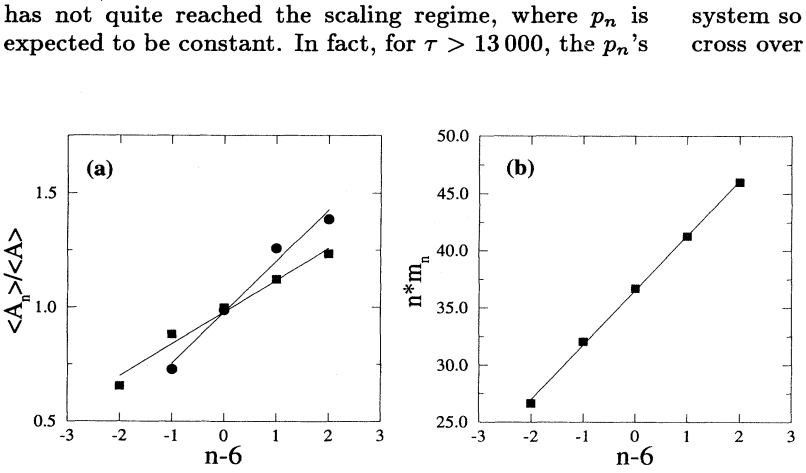

FIG. 16. For run H: (a) Lewis's law for the Voronoi diagram (squares) and for the associated droplet pattern (circles). (b) Aboav-Weaire law. In these plots n is the droplet coordination number and m_n is the average coordination number of the nearest-neighbor droplets of an n-fold droplet. For the square data points, $\langle A \rangle$ and $\langle A_n \rangle$ represent the average area of all Voronoi cells and the average area of n-sided Voronoi cells; for the circular data points they represent the average droplet area and the average area of n-fold coordinated droplets.

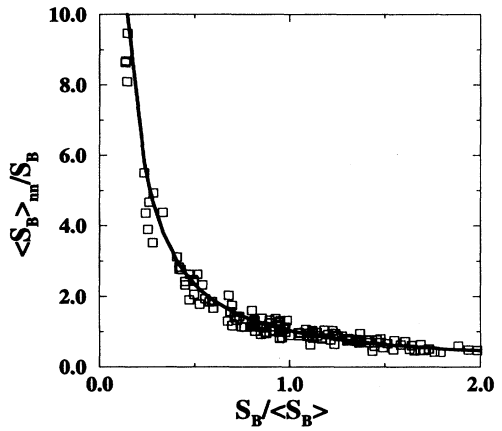

FIG. 17. Spatial correlations in the areas of nearest-neighbor droplets. $\langle S_B \rangle_{NN}$ represents the average area of droplets that are nearest neighbors to a given droplet. The solid line represents Eq. (26) as described in the text.

finite R_{eq} and the system will coarsen forever. The existence of this R_{eq} depends strongly on the model used. A strictly dipolar interaction would predict a finite R_{eq}. For our model, a minimization of the droplet free energy [43,44] shows that if $\beta L^2 > 0.98\sigma(V_f)$ then the equilibrium radius R_{eq} is finite ("noncoarsening" solution). The function $\sigma(V_f)$ is a monotonically increasing function of V_f, with $\sigma(0) = 1$. It has been computed for a dipolar interaction by McConnell [53]. For very thin films, $\sigma(V_f) \simeq 1$. In monolayers the bond number is defined as $N_B = p^2/\sigma$, where p is the dipolar density and σ the surface tension. In the limit of very thin films, it can be expressed in terms of our parameters as $N_B \equiv \beta L^2/2$. This would mean that in a two-dimensional binary mixture, coarsening could be expected for $N_B < 0.49$. However, this number is only indicative since the upper value of N_B below which coarsening is observed will definitely depend on the form of the LRRI kernel. (Notice that $\beta L^2 = 22$, 5, and 0.05 for runs B, I, and H respectively.)

IV. CONCLUSIONS

In this paper we have studied the late-stage kinetics for systems with competing interactions, long-range repulsive and short-range attractive interactions, quenched into the hexagonal phase. Two qualitatively different regimes have been found: a monodisperse hexagonal regime and a polydisperse coarsening regime. In the first regime, at relatively early times, the system becomes monodisperse and can be described as a disordered liquid of equal-sized droplets. The system evolves towards the hexagonal order characteristic of the ground state via collision and annihilation of defects, gaining orientational and translational order in the process. In the coarsening regime, the results of our simulations closely resemble those obtained for a two-dimensional binary mixture confined to an air-water interface. In this regime the system can be described as a two-dimensional froth, with a strong coupling between its topological and geometrical quantities.

[1] C. Kooy and U. Enz, Philips Res. Rep. **15**, 729 (1960).
[2] A.A. Thiele, J. Appl. Phys. **41**, 1139 (1970); Bell Lab. Tech. J. **48**, 3287 (1969).
[3] W.F. Druyvesteyn and J.W. Dorleijn, Philips Res. Rep. **26**, 11 (1971).
[4] J.A. Cape and G.W. Lehman, J. Appl. Phys. **42**, 5732 (1971); J.A. Cape, *ibid.* **43**, 3551 (1972).
[5] T. Garel and S. Doniach, Phys. Rev. B **26**, 325 (1982).
[6] Y. Yafet and E.M. Gyorgy, Phys. Rev. B **38**, 9145 (1988).
[7] A.O. Tsebers and M.M. Maiorov, Magnetohydrodynamics **16**, 21 (1980); A.O. Tsebers, *ibid.* **17**, 113 (1981).
[8] R.E. Rosensweig, M. Zahn, and R. Shumovich, J. Magn. Magn. Mater. **39**, 127 (1983).
[9] S.A. Langer, R.E. Goldstein, and D.P. Jackson, Phys. Rev. A **46**, 4894 (1992).
[10] T. Mitsui and J. Furuichi, Phys. Rev. **90**, 193 (1953).
[11] Reviews are given by C.M. Knobler and R.C. Desai, Annu. Rev. Phys. Chem. **43**, 207 (1992); H.M. McConnell, *ibid.* **42**, 171 (1991); H. Möhwald, *ibid.* **41**, 441 (1990).
[12] D. Andelman, F. Brochard, and J.F. Joanny, J. Chem. Phys. **86**, 3673 (1987).
[13] See, for example, P. de Gennes, *The Physics of Liquid Crystals* (Clarendon Press, Oxford, 1974).
[14] W.L. McMillan, Phys. Rev. B **12**, 1187 (1975).
[15] J.R. Thomsen, W. Cowan, M.J. Zuckermann, and M. Grant, in *Proceedings of the XVIII Winter Meeting On Statistical Physics, Oaxatepo, Mexico, 1989*, edited by A.E. Gonzalez, C. Varea, and M. Medina-Noyola (World Scientific, Singapore, 1989).
[16] L.Q. Chen and A.G. Khachaturyan, Phys. Rev. Lett. **70**, 1477 (1993).
[17] L. Leibler, Macromolecules **13**, 1602 (1980); T. Ohta and K. Kawasaki, *ibid.* **19**, 2621 (1986); Y. Oono and M. Bahiana, Phys. Rev. Lett. **61**, 1109 (1988).
[18] C.A. Murray and D.H. Van Winkle, Phys. Rev. Lett. **58**, 1200 (1987); C.A. Murray and R.A. Wenk, *ibid.* **62**, 1643 (1989); C.A. Murray, W.O. Sprenger, and R.A. Wenk, Phys. Rev. B **42**, 688 (1990).
[19] D.M. Petrich and R.E. Goldstein, Phys. Rev. Lett. **72**, 1120 (1994); Q. Ouyang and H.L. Swinney, Nature (London) **352**, 610 (1991).
[20] C. Roland and R.C. Desai, Phys. Rev. B **42**, 6658 (1990).
[21] R.C. Desai, C. Sagui, and K.R. Elder, in *Structure and Dynamics of Strongly Interacting Colloids and Supramolecular Aggregates in Solution*, edited by S.H. Chen *et al.* (Kluwer, Dordrecht, 1992), p. 205.
[22] C. Sagui and R.C. Desai, Phys. Rev. E **49**, 2225 (1994).
[23] C. Sagui and R.C. Desai, Phys. Rev. Lett. **71**, 3995 (1993).
[24] M. Seul, N.Y. Morgan, and C. Sire, Phys. Rev. Lett. **73**, 2284 (1994); M. Seul, Europhys. Lett. **28**, 557 (1994);

N.Y. Morgan and M. Seul, J. Phys. Chem. **99**, 2088 (1995); C. Sire and M. Seul, J. Phys. (France) I **5**, 97 (1995).

[25] J.M. Kosterlitz and D.J. Thouless, J. Phys. C **6**, 1181 (1973); in *Progress in Low Temperature Physics*, edited by D.F. Brewer (North-Holland, Amsterdam, 1978), Vol. VII-B, p. 373.

[26] B.I. Halperin and D.R. Nelson, Phys. Rev. Lett. **41**, 121 (1978); D.R. Nelson and B.I. Halperin, Phys. Rev. B **19**, 2457 (1979); **21**, 5312 (1980).

[27] A.P. Young, Phys. Rev. B **19**, 1855 (1979).

[28] D.R. Nelson, M. Rubinstein, and F. Spaepen, Philos. Mag. A **46**, 105 (1982).

[29] C.C. Grimes and G. Adams, Phys. Rev. Lett. **42**, 795 (1979).

[30] R.J. Birgeneau and J.D. Litster, J. Phys. (Paris) Lett. **38**, 1399 (1978); D.E. Moncton and R. Pindak, Phys. Rev. Lett. **43**, 701 (1979); J.D. Brock, A. Aharony, R.J. Birgeneau, K.W. Evans-Lutterodt, J.D. Litster, P.M. Horn, G.B. Stephenson, and A.R. Tajbakhsh, *ibid.* **57**, 98 (1986).

[31] K.J. Strandburg, Rev. Mod. Phys. **60**, 161 (1988). See also *Bond-Orientational Order in Condensed Matter Systems*, edited by K.J. Strandburg (Springer, New York, 1992).

[32] C.A. Murray, P.L. Gammel, D.J. Bishop, D.B. Mitzi, and A. Kapitulnik, Phys. Rev. Lett. **64**, 2312 (1990); D.G. Grier, C.A. Murray, C.A. Bolle, P.L. Gammel, D.J. Bishop, D.B. Mitzi, and A. Kapitulnik, *ibid.* **66**, 2270 (1991).

[33] R. Seshadri and R.M. Westervelt, Phys. Rev. Lett. **66**, 2774 (1991); Phys. Rev. B **46**, 5142 (1992); **46**, 5150 (1992).

[34] M. Seul and C.A. Murray, Science **262**, 558 (1993); M. Seul, J. Phys. (France) I **4**, 319 (1994).

[35] D.R. Nelson, in *Phase Transitions and Critical Phenomena*, edited by C. Domb and J. K. Lebowitz (Academic Press, New York, 1983), Vol. 7.

[36] D. Weaire and N. Rivier, Contemp. Phys. **25**, 59 (1984).

[37] M.O. Magnasco, Philos. Mag. B **65**, 895 (1992).

[38] F.T. Lewis, Anat. Rec. **38**, 341 (1928); Am. J. Bot. **30**, 766 (1943).

[39] N. Rivier, J. Phys. (Paris) Colloq. **43**, C9-91 (1982); N. Rivier and R. Lissowski, J. Phys. A **15**, L143 (1982).

[40] M.P. Allen and D.J. Tildesley, *Computer Simulations of Liquids* (Clarendon Press, Oxford, 1992).

[41] D. Frenkel and J.P. McTague, Phys. Rev. Lett. **42**, 1632 (1979).

[42] C.W.J. Beenakker, Phys. Rev. Lett. **57**, 2454 (1986); M. Marder, Phys. Rev. A **36**, 438 (1987).

[43] C. Sagui and R.C. Desai, Phys. Rev. Lett. **74**, 1119 (1995).

[44] C. Sagui and R.C. Desai, Phys. Rev. E **52**, 2822 (1995).

[45] R. Loft and T.A. DeGrand, Phys. Rev. B **35**, 8528 (1986).

[46] H. Toyoki, Phys. Rev. A **42**, 911 (1989).

[47] A.N. Pargellis, P. Finn, J.W. Goodby, P. Pannizza, B. Yurke, and P.E. Cladis, Phys. Rev. A **46**, 7765 (1992).

[48] B. Yurke, A.N. Pargellis, T. Kovac, and D. Huse, Phys. Rev. E **47**, 1525 (1993).

[49] M. Mondello and N. Goldenfeld, Phys. Rev. A **42**, 5865 (1990).

[50] T.M. Rogers and R.C. Desai, Phys. Rev. B **39**, 11956 (1989).

[51] K.B. Lauritsen, C. Moukarzel, and H.J. Herrmann, J. Phys. (France) I **3**, 1941 (1993).

[52] M. Blanc and A. Mocellin, Acta Metall. **21**, 149 (1979).

[53] H.M. McConnell, Proc. Natl. Acad. Sci. **86**, 3452 (1989).

For our interaction, $\sigma(V_f)$ also depends weakly on the film thickness.